NJC

PAPER

View Article Online
View Journal | View Issue

Check for updates

Cite this: *New J. Chem.*, 2024, **48**, 17500

Enhanced visible-light photocatalytic degradation of organic pollutants using fibrous silica titania and Ti_3AlC_2 catalysts for sustainable wastewater treatment†

Samia,[a] Muhammad Usman,[bd] Ahmed I. Osman, *[c] Khurram Imran Khan, [d] Faiq Saeed,[e] Yilan Zeng,[fg] Martin Motola [f] and Haitao Dai*[a]

Received 22nd July 2024,
Accepted 27th August 2024

DOI: 10.1039/d4nj03277b

rsc.li/njc

Visible light photocatalysis offers a green and sustainable approach to wastewater treatment and environmental remediation. This study focuses on the synthesis of fibrous silica titania (FST) *via* a green method and comprehensively evaluates its photocatalytic performance compared with Ti_3AlC_2 powder. X-ray diffraction (XRD) and scanning electron microscopy (SEM) revealed superior crystallinity and unique lamellar structures in FST, contributing to its enhanced photocatalytic activity. The FST catalyst achieved remarkable degradation efficiencies of 93% for MB and 96% for rhodamine B (RB) under visible light, outperforming the bare Ti_3AlC_2 powder. This promising performance is attributed to FST's narrow band gap (∼2.98 eV), high surface area, and minimal photogenerated charge carrier recombination. Kinetic studies showed excellent agreement with pseudo-first-order kinetics, with R^2 values of 0.9801 and 0.988 for MB and RB, respectively. Reusability tests demonstrated sustained efficiency, with degradation rates remaining above 80% after four cycles. GC-MS analysis identified intermediates formed during photocatalytic degradation, ultimately converting them into harmless products, *i.e.*, CO_2 and H_2O. These findings highlight FST as an economical, sustainable, and efficient photocatalyst for organic pollutant degradation compared to Ti_3AlC_2.

1. Introduction

Water pollution and the availability of fresh and clean water are among the global concerns of this era. The rapid and largely uncontrolled growth of industries and urbanization has exacerbated these issues, leading to significant challenges in maintaining water quality and accessibility.[1–3] Several industries, including the textile industry, release large volumes of organic pollutants into water bodies, which may have detrimental effects on various forms of living organisms.[4,5] These discharges often contain large volumes of dyes, many of which are non-biodegradable and detrimental to the environment.[6,7] These wastewaters are often treated with varying degrees of success, using a variety of cutting-edge processes like adsorption, biodegradation, coagulation, flocculation, electrocoagulation, *etc.*[8–10] The chromophore components of dyes may be destroyed to different extents in these physio-chemical processes, resulting in their partial or total mineralization.[11]

However, several biological, physical, and chemical methods have all been employed in the past to remove impurities like textile colors from water.[12] Among the physical and chemical techniques used in the many advanced treatment strategies are nanofiltration, ultrasonic decomposition, electrocoagulation, adsorption, chemical coagulation, enhanced chemical oxidation, and sedimentation.[6,13,14] However, most of these systems produce expensive secondary pollutants and consume large amounts of energy.[15] Over the past decade, researchers have focused much on the photocatalytic degradation of organic

---

[a] Tianjin Key Laboratory of Low Dimensional Materials Physics and Preparing Technology, School of Science, Tianjin University, Tianjin 300072, China. E-mail: htdai@tju.edu.cn

[b] Center of Excellence on Catalysis and Catalytic Reaction Engineering, Department of Chemical Engineering, Faculty of Engineering, Chulalongkorn University, Bangkok 10330, Thailand

[c] School of Chemistry and Chemical Engineering, Queen's University Belfast, David Keir Building, Stranmillis Road, Belfast, BT9 5AG, Northern Ireland, UK. E-mail: aosmanahmed01@qub.ac.uk

[d] Faculty of Materials and Chemical Engineering, Ghulam Ishaq Khan Institute of Engineering Sciences and Technology, Topi, Swabi, Pakistan

[e] Tianjin Key Laboratory of Molecular Optoelectronic Science, Department of Chemistry, School of Science, Tianjin University, Tianjin 300072, China

[f] Department of Inorganic Chemistry, Faculty of Natural Sciences, Comenius University Bratislava, Mlynska Dolina, Ilkovicova 6, 842 15 Bratislava, Slovakia

[g] Department of Environmental Ecology and Landscape Management, Faculty of Natural Sciences, Comenius University Bratislava, Mlynska Dolina, Ilkovicova 6, 842 15 Bratislava, Slovakia

† Electronic supplementary information (ESI) available. See DOI: https://doi.org/10.1039/d4nj03277b

pollutants as a potentially effective method for removing hazardous materials and textile dyes from untreated sewage.[16]

Currently, the most efficient way for breaking down and mineralizing organic wastewater in the environment is through heterogeneous photocatalysis by semiconductors.[17,18] Titanium dioxide (TiO_2) is a well-known semiconductor that offers strong chemical and physical stability together with excellent photocatalytic activity. However, TiO_2 has certain drawbacks, such as a low surface area that may result in pore size limits.[19] To address this issue, extensive research has been conducted on developing TiO_2 nanostructures, including nanoparticles, nanotubes, nanorods, nanofibers, and nanoflowers. It has been demonstrated that the formation of nanostructures in TiO_2 can overcome the reaction's diffusion restriction.[20] Lately, a novel method using soft templating employing a surfactant that enables the formation of mesopores and micropores with a dendrimer-like silica fiber architecture[21] enhances the accessibility of active sites, thereby improving the photocatalytic activity through the addition of dendrimer-like silica fibers.[22]

Many studies have been conducted recently to prepare more selective and efficient structured photocatalysts.[23] Within this framework, Ti_3AlC_2 has been studied as a two-dimensional (2D) layered ternary carbide material belonging to the MAX phase, where M represents early transition elements, A is an A group element, and X is either C or N.[24] These materials exhibit remarkable potential for enhancing the efficiency of less efficient photocatalysts. The values of n can be 1, 2, or 3, denoting the MAX phases 211, 312, and 413, correspondingly.[25] Two-dimensional close-packed Al planes with three Ti layers stacked by each Al plane and alternate stacking of edge-shared Ti_6C octahedra make up their crystal structure. MAX phases combine the desirable properties of metals and ceramics, displaying traits that make them both appealing and useful,[26] offering heat shock resistance, corrosion resistance, excellent machinability, high electrical conductivity, and extremely low friction. Ti_3AlC_2 exhibits a remarkable electrical structure and a greater exposed surface area within the MAX phase, making it suitable for energy, electronic, and photocatalytic applications.[27] With their metallic qualities, stability at high temperatures, and outstanding mechanical capabilities, MAX phase solids may be used in a variety of applications beyond energy and electronics.[28] While a considerable amount of research has been carried out on the photocatalytic use of etching Ti_3AlC_2 into Ti_3C_2, less attention has been paid to the use of Ti_3AlC_2-MAX phase solids in photocatalysis.[29] Research on CO_2 reduction by methane bio-reforming using just the MAX phase has been reported.[30] Due to its layered structure and effective charge separation, Ti_3AlC_2 shows great potential for photocatalytic H_2 generation.[31] Comparative studies between fibrous silica-titania and the Ti_3AlC_2-MAX phase are expected to identify strategies for reducing charge carrier recombination and enhancing dye degradation.[26]

Thus, employing a microemulsion technique, we have successfully produced fibrous silica loaded with titania (FST) under microwave irradiation. This FST demonstrated outstanding activity in the photodegradation of methylene blue (MB) and rhodamine B (RB) when exposed to visible light. The FST catalyst offers a high fiber density and high active site availability; the photogenerated charge carrier recombination rate in FST is also low as compared to that in Ti_3AlC_2 powder. As far as we are aware, no studies have been published on the comparative analysis between fibrous silica-titania and the Ti_3AlC_2 Max-phase for the degradation of MB and RB. The catalysts were characterized using XRD, FE-SEM, TEM, UV-Vis DRS, FTIR, XPS, and PL. The narrow band gap of FST provides better photocatalytic activity under the irradiation of visible light. The FST photocatalyst provided a significant degradation efficiency of 93% and 96%, respectively.

In recent years, the development of advanced photocatalysts has garnered significant attention due to their potential in environmental remediation. Among the photocatalysts, fibrous silica loaded with titania (FST) has emerged as a promising candidate. Utilizing a microemulsion technique under microwave irradiation, we successfully synthesized FST, which demonstrated remarkable efficiency in the photodegradation of organic dyes such as MB and RB under visible light. This high-performance catalyst benefits from its high fiber density and abundant active sites, leading to a lower recombination rate of photogenerated charge carriers compared to conventional Ti_3AlC_2 powder. Despite the promising results, there is a notable gap in the literature regarding comparative studies of FST and Ti_3AlC_2 MAX-phase materials for dye degradation. This article aims to provide a comprehensive understanding of their structural and functional properties, highlighting their potential as an efficient and cost-effective solution for wastewater treatment.

2. Materials and methods

All materials used in this study were of analytical grade with the highest purity. Deionized water was utilized as the solvent. Tetraethyl orthosilicate (TEOS), butyl alcohol, toluene, and cetyltrimethylammonium bromide (CTAB) were purchased from Merck Sdn., Tianjin, China. $CO(NH_2)_2$ and Na_2SO_4 are from Tianjin, China. Pure commercial titania (JRC TiO_2) 99%, titanium (metal basis powder −325 mesh, 99.99%), titanium carbide (TiC 99.5%), and aluminum (mesh size −40 + 325, 99.8%) were purchased from Tianjin, China. Methylene blue, and rhodamine B 99% were acquired from Tianjin, China.

2.1. Synthesis of fibrous silica titania (FST)

Catalyst FST was produced utilizing a microemulsion process, as previously reported in the literature[32,33] and depicted in Fig. 1. A homogenous mixture containing 5.8271 g of cetyltrimethylammonium bromide (CTAB), 173 mL of deionized water, and 3.4819 g of urea was thoroughly mixed in a 500 mL beaker for 20 min at room temperature while stirring at a speed of 800 to 900 rpm. In addition, 10 mL of butanol and 200 mL of toluene were added, and the mixture was rapidly agitated for 15 min. TiO_2 seeds (1.44 g) were added to the above mixture

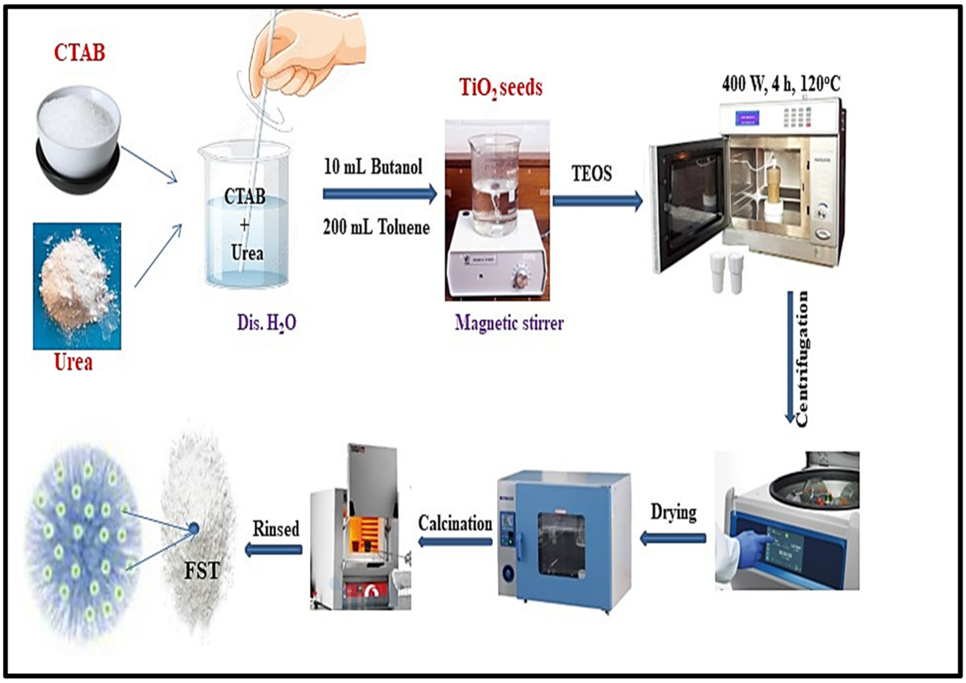

Fig. 1 Schematic diagram of the synthesis route of fibrous silica titania (FST).

and were vigorously stirred for another 30 min. Subsequently, 13.15 mL of tetraethyl orthosilicate was added to the mixture and aggressively agitated for the next 2 h to improve the composition. The obtained solution was subjected to hydrothermal treatment for the next 4 h at 120 °C under 400 W microwave irradiation. The resulting solution was centrifuged, washed with distilled water and acetone several times, and then dried at 80 °C overnight to form a white precipitate. The as-prepared material was calcined at 550 °C for 3 h to obtain FST.

2.2. Synthesis of Ti_3AlC_2

Titanium (metal basis powder −325 mesh, 99.99%), titanium carbide (TiC 99.5%), and aluminum (mesh size −40 + 325, 99.8%) were purchased from Tianjin, China. 3 moles of titanium, 1 mole of aluminum, and 2 moles of carbon were stirred for 30 minutes. Powders were mechanically mixed in a ball mill to obtain a homogenous mixture without any agglomerates. This mixture was then vacuum-packed into a glass container. Afterwards, Ti_3AlC_2 synthesis occurred through sintering under an argon atmosphere at 1450 °C for 2 hours in a furnace, effectively yielding the desired powders.

2.3. Characterization

XRD (Bruker AXS, D8-S4) was employed to determine the crystalline structure of the synthesized samples. A field-emission scanning electron microscope (FSEM; Hitachi, S-8100) and a transmission electron microscope (TEM, JEM-2100F) were utilized to investigate the morphological aspects and microstructures. FTIR spectroscopy using a PerkinElmer spectrum (GX FT) Spectrometer was used to investigate the functional groups. X-ray photoelectron spectroscopy (XPS) was used to measure the chemical oxidation and electron mobility of the as-synthesized FST and Ti_3AlC_2 photocatalyst and was conducted on a Shimadzu Axis Ultra Dld spectrometer outfitted through an Al X-ray source with binding energies ranging from 0 to 800 eV. PL spectra were obtained using a Jonin-Yvon-Fluorolog spectrofluorimeter to measure the rate of recombination of photogenerated charge separation carriers. UV-vis DRS in the range of 200–800 nm (PerkinElmer, L750) was used to measure the absorbance spectra and band gap of FST and Ti_3AlC_2 powder catalyst. The surface area was examined using the BET instrument 3H-2000 PS2. ESR signals were noted using an electron spin resonance (ESR) spectrometer (JEOL, JES-FA200) to examine the paramagnetic species.

2.4. Photocatalytic activity evaluation

Photocatalytic performance for the degradation of MB and RB was examined using the as-synthesized FST and Ti_3AlC_2 powder samples under irradiation of a 300 W xenon lamp, with a wavelength of $\geq$400 nm. 100 mg of the sample was uniformly spread into a beaker containing 20 ppm MB solution and kept on stirring in the dark for 30 min to obtain the adsorption–desorption equilibrium. There was no noticeable decrease in the concentration of MB and RB observed under the dark conditions. Once the equilibrium is obtained, the light is turned on, and a sample of 3 mL is collected for every 30 min interval to separate the precipitates from the MB and RB solution. A UV-vis spectrophotometer Shimadzu UV-2200 was used to measure the absorption peak intensity of MB and RB occurring at 664 nm and 567 nm under visible light irradiation. The acuity of the MB and RB absorption peaks gradually and slowly reduces with increasing degradation time. Precipitates collected were washed several times with distilled water and specifically collected for the recyclability test. The UV-vis absorption peaks showed that the maximum MB and RB absorption wavelength moved with an accumulative dye degradation time from 0 to 120 min. The degradation efficiency was calculated using eqn (1).

$$R\,(\%) = \frac{C_o - C}{C_o} \times 100 \qquad (1)$$

3. Results and discussion

3.1. Characterization of photocatalysts

The purity of phase and crystalline structure of synthesized FST and Ti_3AlC_2 powder were investigated, and their XRD patterns are presented in Fig. 2. Diffractions of FST were observed at 25.6°, 37.9°, 48.4°, 55.45° and 62.8° 2θ, which are attributed to the (101), (004), (200), (105), and (204) planes, respectively (JCPDS file no. 00-004-0477).[34,35] A small distinct diffraction was observed at $2\theta°$ of 54.32°, which reflects the presence of SiO_2 in FST, and hence the successful fabrication of the FST catalyst was confirmed.[36] FST diffractions are slightly noisy and low in intensity, which might be due to the minor loss in their structure while maintaining the main diffractions of the TiO_2 anatase/rutile phase and due to the formation of dendrimeric silica fibers surrounding the TiO_2.[37] For the pristine Ti_3AlC_2 powder, the diffractions were observed at 34.2°, 36.9°, 39.1°, 41.9°, 48.5°, 56.4°, 60.27°, 70.43° and 73.91°, which corresponded with the planes (101), (103), (104), (105), (107), (109), (110), (1012) and (118), respectively.[38] Consequently, this high crystalline structure of Ti_3AlC_2 powder confirms the presence of small TiO_2 nanoparticles on the surface of Ti_3AlC_2, which is due to the presence of the rutile and anatase phase of TiO_2 formation in the crystal structure of Ti_3AlC_2.[39] Fig. S1 (ESI†) presents the FT-IR spectra of the synthesized FST and Ti_3AlC_2 powder samples. For the FST sample, sharp absorption peaks shown at 465.17 cm^{-1} and 1098.69 cm^{-1} are typically associated with metal–oxygen bending vibrations and Si–O–Si asymmetric stretching vibrations, respectively. These characteristics suggest a well-structured silica matrix with embedded metal oxides, which are critical for catalytic activity due to their role in facilitating electron transfer and enhancing adsorption sites for reactants. Such a structure is essential for applications requiring high chemical stability and mechanical strength. The broad peak at 2165.40 cm^{-1} in the FST spectrum suggests the presence of C–H stretching vibrations, likely from organic residuals or surface modifications, which indicates that the surface chemistry has been engineered to include organic functionalities that can improve interaction with organic pollutants in environmental remediation. In contrast, the spectrum of Ti_3AlC_2 shows fewer distinct peaks, suggesting a simpler surface chemistry with fewer active sites for chemical

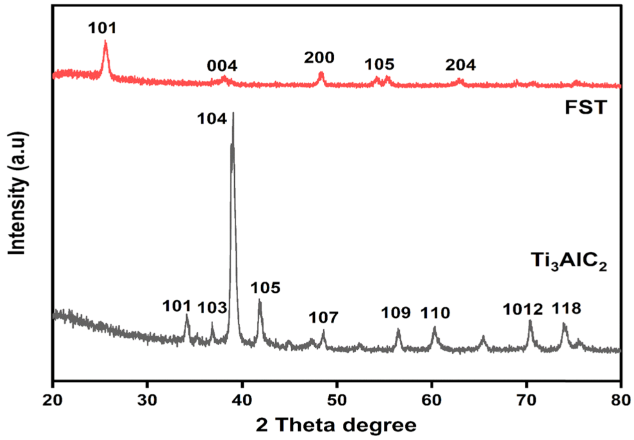

Fig. 2 XRD patterns of FST and Ti_3AlC_2 powder catalysts.

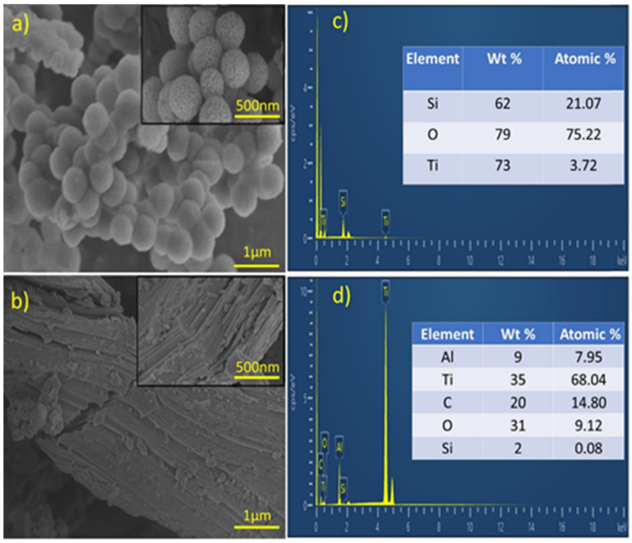

Element	Wt %	Atomic %
Si	62	21.07
O	79	75.22
Ti	73	3.72

Element	Wt %	Atomic %
Al	9	7.95
Ti	35	68.04
C	20	14.80
O	31	9.12
Si	2	0.08

Fig. 3 Surface morphology of FST (a) and Ti_3AlC_2 powder (b) along with the EDX spectra of FST and Ti_3AlC_2 powder catalysts (c) and (d).

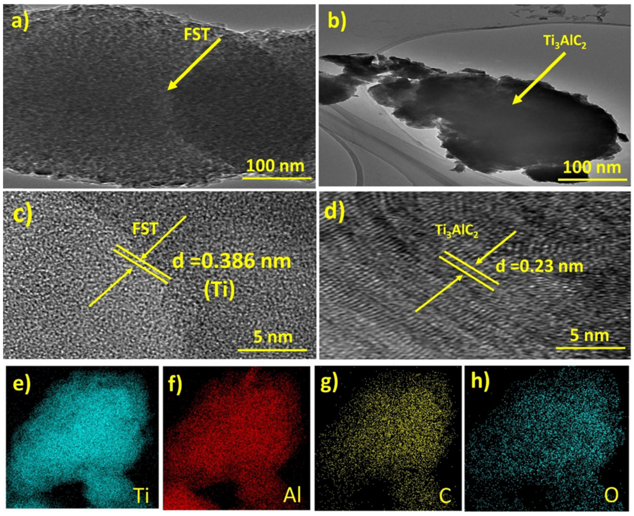

Fig. 4 TEM images of FST (a) and Ti_3AlC_2 powder (b), HR TEM images FST and Ti_3AlC_2 powder (c and d) along with the elemental mapping of the Ti_3AlC_2 powder catalyst (e–h).

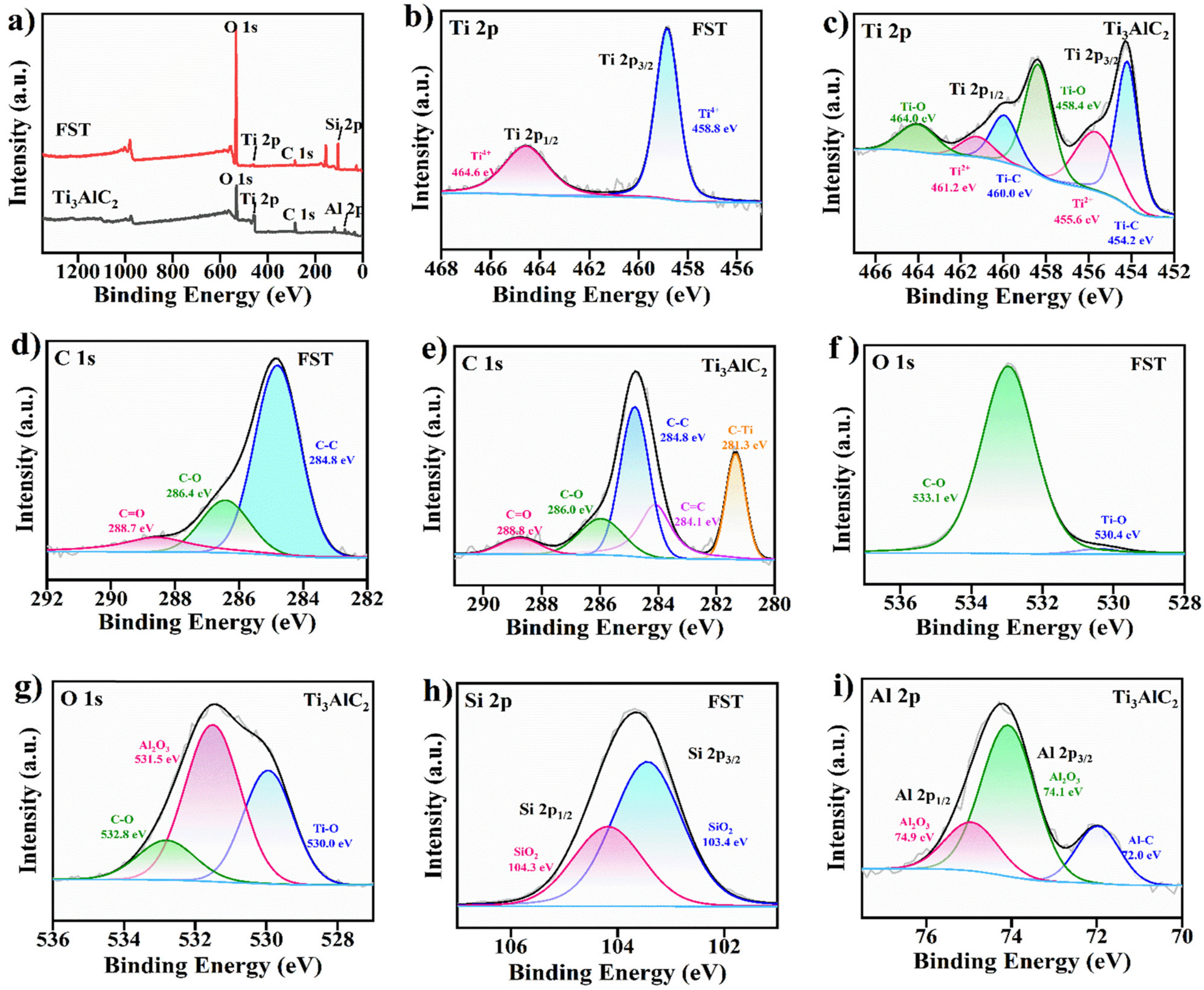

Fig. 5 XPS spectra of (a) FST and Ti_3AlC_2 powder, (b) and (c) Ti 2p spectra, (d) and (e) C 1s spectra, (f) and (g) O 1s spectra, and (h) and (i) Si 2p spectrum and Al 2p spectrum of FST and Ti_3AlC_2 powder, respectively.

reactions, which may result in different catalytic reactivities and efficiencies. This contrast highlights that variations in the presence and intensity of specific vibrational modes directly relate to how each material interacts with chemical species, affecting their suitability and performance in catalysis and environmental remediation applications.

The surface morphology and microstructure were examined for the synthesized FST and Ti_3AlC_2 powder catalysts utilizing scanning electron microscopy (SEM) and transmission electron microscopy (TEM), as depicted in Fig. (3) and (4), respectively. Fig. 3(a) presents the SEM image of FST, which clearly shows the cocks-comb like structure of the FST nanospheres with their size ranging between 300 and 600 nm, which is attributed to the formation of dendrimeric fibrous FST with SiO_2 and the anatase phase of TiO_2.[35,40] Fig. S2 (ESI†) presents the elemental mapping of the FST catalyst. Fig. 3(b) shows the morphology of Ti_3AlC_2 as spherical particles, densely packed and compressed thin sheets, confirming the significant interlayer spacing of particles and the successful formation of Ti_3AlC_2 powder.[31] The light absorption of Ti_3AlC_2 in the visible range is due to its dark color, but the layered structure has hole defects caused by some Ti and Al layers being etched away, providing vacant spaces to aid in photocatalytic degradation of MB and RB.[41] Fig. 3(c) and (d) shows energy dispersive X-ray analysis, confirming the uniform dispersion of all the elements in both FST and Ti_3AlC_2 without any impurity. Fig. S3 (ESI†) represents the elemental mapping of the Ti_3AlC_2 catalyst.

Fig. 4(a) shows the TEM image of FST, revealing spherical shapes and dendrimer fibers, which can provide more access to the active sites, and a *d*-spacing of 0.386 nm aligned with the (101) plane of anatase phase TiO_2 Fig. 4(c).[42] Moreover, the dendrimer fiber structure of FST is produced from amorphous SiO_2 and the anatase phase of TiO_2, which is also confirmed by the SEM results of FST depicted in Fig. 3(a).[32] Fig. 4(b) presents the microstructure of Ti_3AlC_2 with the multilayer sheets compact with each other and with a *d*-spacing of 0.23 nm see Fig. 4(d), which can be helpful in the photocatalytic degradation of MB and RB, consistent with the literature.[43] The elemental mapping results of Ti_3AlC_2 shown in Fig. 4(e–h) confirm the uniform dispersion of Ti, Al, C, and O elements in the sheet-like structure of Ti_3AlC_2.

XPS was employed to further analyze the chemical oxidation state and electron migration of FST and Ti_3AlC_2 powder. As depicted in Fig. 5(a), the survey scan of deconvoluted O 1s spectra of FST exhibited three peaks at 527.6, 530, and 531.4 eV, corresponding to lattice oxygen, surface hydroxyl groups (–OH), and adsorbed oxygen, respectively.[44] Additionally, the composition of Ti_3AlC_2, comprising Ti, Al, C, and O elements, was confirmed by a single survey spectrum shown in Fig. 5(a). A red shift in the binding energies of FST suggests photogenerated electron transfer from SiO_2 to TiO_2, leading to a strong interaction between Si and Ti in FST.[45] Fig. 5(b) and (c) illustrates the high-resolution spectrum of Ti 2p for FST and Ti_3AlC_2, respectively. The Ti 2p spectra of FST were deconvoluted into four peaks, as illustrated in Fig. 5(b). The peaks at 456.1 and 458.7 eV are attributed to Ti^{3+} $2p^{3/2}$ and Ti^{4+} $2p^{3/2}$, respectively.[33] The high-resolution Ti 2p XPS spectra of Ti_3AlC_2 powders shown in Fig. 5c exhibit three characteristic peaks, corresponding to the Ti–C $2p^{3/2}$, Ti–C $2p^{1/2}$, and Ti–O orbitals, respectively, and are well consistent with the existing literature.[46] From the analysis of XPS data, Fig. 5(d) and (e) displays the high-resolution XPS spectral peaks of C 1s. The peaks at 286.0 and 288.7 eV correspond to the C–O and C═O bonds. A distinct peak was observed in the Ti_3AlC_2 powder sample at 281.3 eV, which was attributed to the C–Ti bonding orbitals.[31] Fig. 5(f) and (g) represents the O 1s for both FST and Ti_3AlC_2 powder materials. A distinct peak was observed at 531.5 eV, which was due to Al_2O_3, hence confirming the successful synthesis of Ti_3AlC_2 powder, as reported in the previous research.[31] The Si 2p spectra of FST are depicted in Fig. 5(h). The deconvoluted peaks of FST at 104.3 and 103.4 eV both correspond to Si–O–Si,[47] which are highly correlated to the results of the FTIR spectra (Fig. S1, ESI†). Conversely, the high-resolution Al 2p XPS spectra of Ti_3AlC_2 powders exhibit three distinct characteristic peaks, corresponding to the Al-$2p^{3/2}$, Al $2p^{1/2}$, and Al–O orbitals, with binding energies of 74.1, 74.9 and 72.0 eV, respectively.[48] Typically, a shift in binding energy in the XPS spectra indicates a significant interfacial interaction between the various components. Fig. S5 (ESI†) displays the valence band spectra of both FST and Ti_3AlC_2, offering insights into the density of electronic states and energy distribution. From the graph, it's clear that Ti_3AlC_2 has a pronounced peak at around 0.32 eV, indicative of a higher electronic density at this energy, whereas the FST spectrum starts to increase significantly only after 4.81 eV, suggesting a lower density of states near the Fermi level. This difference in electronic structure, as evident from the valence band spectra (Fig. S5, ESI†), correlates with the shifts observed in the binding energies of the XPS spectra (Fig. 5). The presence of Ti^{3+} $2p^{3/2}$ and Ti^{4+} $2p^{3/2}$ states in FST and the various chemical environments of C and Al in Ti_3AlC_2 as deduced from the high-resolution C 1s and Al 2p spectra support the interpretation that Ti_3AlC_2 has a more complex electronic environment. These spectral differences are likely due to the different elemental compositions and chemical bonding environments in FST and Ti_3AlC_2, reinforcing the findings of substantial interfacial interactions and electron transfer phenomena observed in the XPS analysis.

The nitrogen adsorption/desorption isotherms (Fig. 6) for both FST and Ti_3AlC_2 materials revealed significant insights into their surface properties, exhibiting typical characteristics of mesoporous structures. The FST material demonstrated a type IV isotherm, indicative of mesoporous materials. The Brunauer–Emmett–Teller surface area, pore volume and average pore size of FST and Ti_3AlC_2 are shown in Table 1. These values indicate the distinct differences in the pore structures

Table 1 BET analysis of FST and Ti_3AlC_2

	Pore volume (cm^3 g^{-1})	Average pore size (nm)	Surface area (m^2 g^{-1})
FST	0.3363	3.9760	338.2070
Ti_3AlC_2	0.0120	24.7627	1.9384

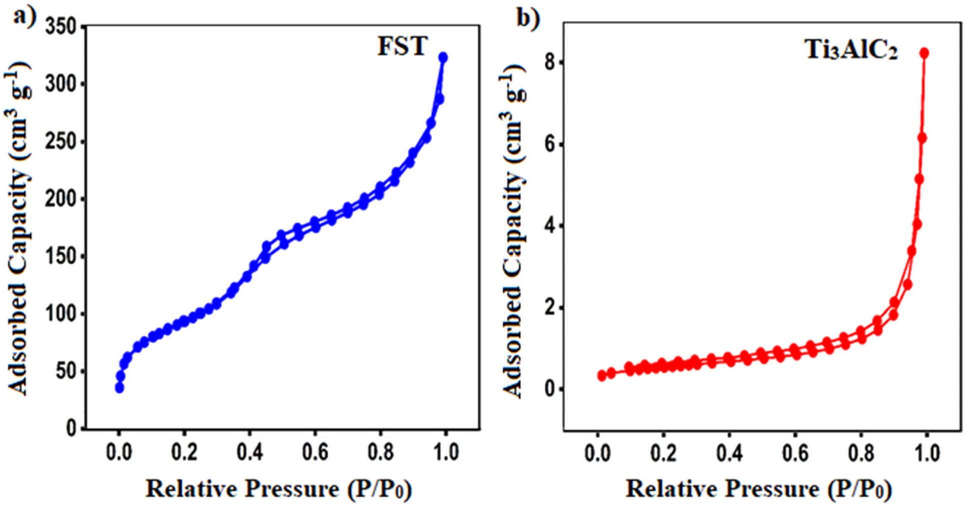

Fig. 6 N_2 adsorption–desorption isotherms of (a) FST and (b) Ti_3AlC_2.

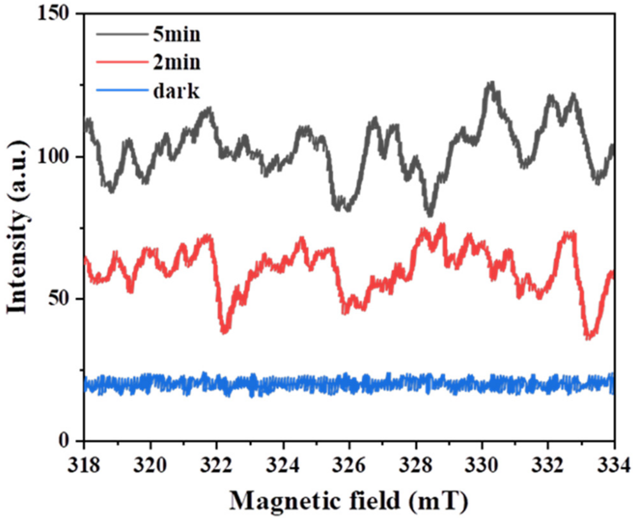

Fig. 7 Electron spin resonance spectra of FST under various light conditions.

and surface areas of FST and Ti_3AlC_2 materials, underscoring their potential applications. The FST material, with its high surface area and uniform mesoporous structure, is ideal for applications requiring extensive surface interactions, such as in catalysis and gas adsorption. The moderate BET constant (C = 102.3) also indicated balanced adsorption energy, beneficial for dynamic adsorption processes.

On the other hand, the Ti_3AlC_2 material, with its lower surface area and larger pore size, may be more suited for applications where the diffusion of larger molecules is required, such as in certain types of catalysis or filtration processes; the higher BET constant (C = 126.0) suggested stronger interactions between the adsorbate and the surface, which can be advantageous in applications where stronger adsorption bonds are desired.

3.1.1. ESR analysis. The ESR spectrum (Fig. 7) exhibits the strongest response with 5-minute light exposure, displaying prominent peaks that likely indicate the formation of stable free radicals or paramagnetic centers under illumination. The diminished signal intensity after 2 minutes and the nearly absent signal under dark conditions suggest dynamic changes in photogenerated free radicals or charge carriers. Such behavior is crucial for photocatalytic materials, as the activity and stability of the catalysts directly depend on their ability to

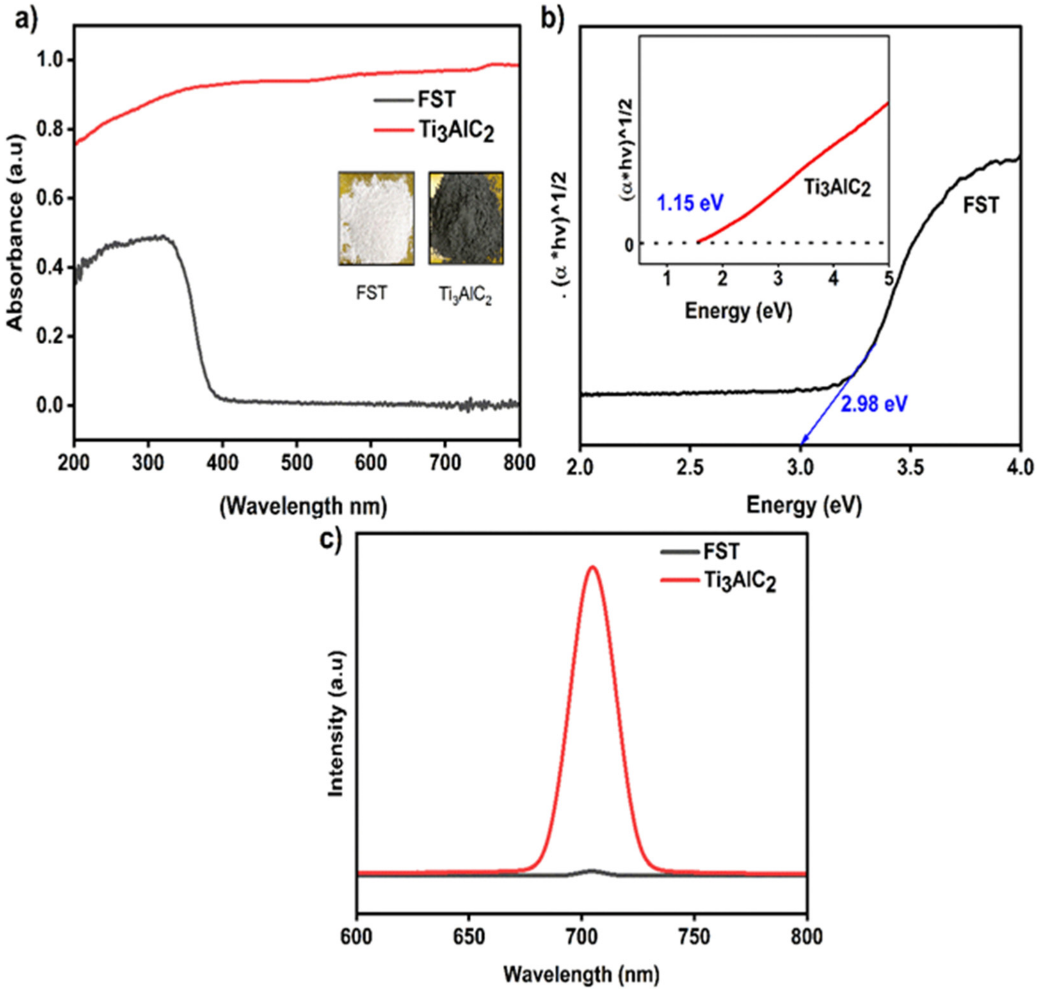

Fig. 8 (a) UV-vis DRS spectrum and (b) and (c) corresponding band gap alignment and PL emission spectra of FST and Ti_3AlC_2 powder.

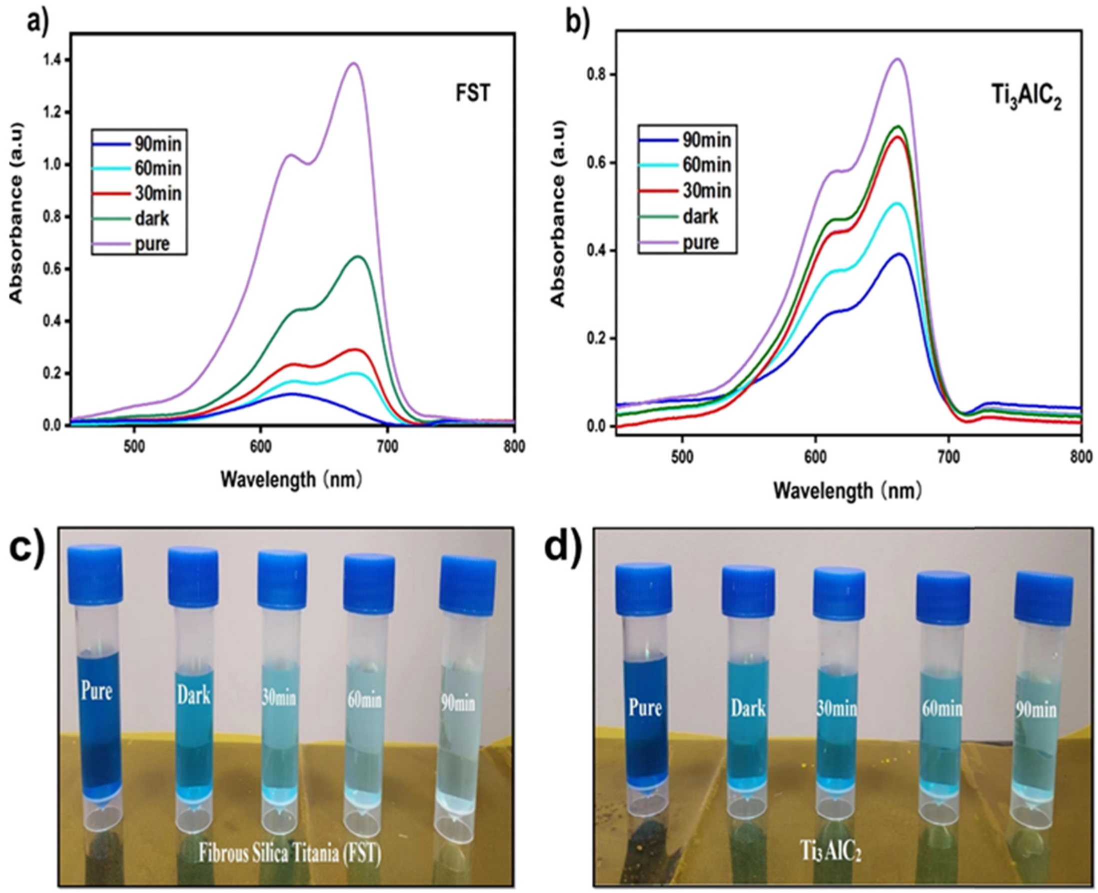

Fig. 9 UV-vis absorption spectra of (a) and (c) FST and (b) and (d) Ti_3AlC_2 powder catalysts for MB.

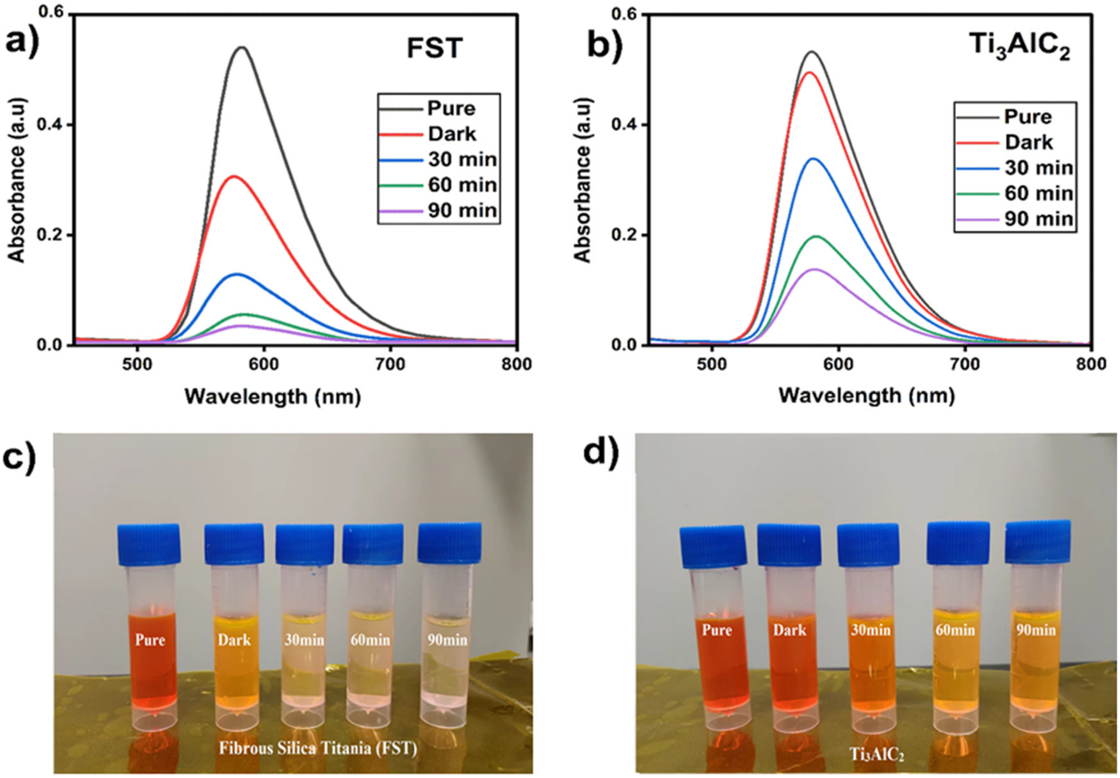

Fig. 10 UV-vis absorption spectra of (a) and (c) FST and (b) and (d) Ti_3AlC_2 powder catalysts for RB.

generate and maintain reactive species under light exposure. This dynamic behavior, indicated by ESR, underscores the potential in applications such as pollutant degradation or energy conversion, where controlled radical generation is the key factor.

3.2. Optical properties

Light absorption properties and characteristics were analyzed *via* UV-vis DRS for pristine FST and Ti_3AlC_2 powder samples to calculate the variation in the optical properties. As depicted in Fig. 8(a), the results reveal distinct patterns. Pristine FST exhibits absorbance spectra peaking at approximately 420 nm, suggesting an inclination towards absorbing light in the visible spectrum. In contrast, Ti_3AlC_2 shows no discernible absorbance spectra within the wavelength range of 200 to 800 nm, consistent with its metallic nature. However, its dark color signifies its ability to absorb visible light irradiation.[49]

The band gap energy was determined for both FST and Ti_3AlC_2 using eqn (2) *via* the Tauc plot method:

$$\alpha h\nu = A(h\nu - E_g)n/2 \qquad (2)$$

Here, α represents the absorption coefficient, $h\nu$ is Planck's energy, E_g denotes the band gap energy, and A is a proportionality constant. The type of transition is denoted by n, with values typically being 1 for direct transitions and 2 for indirect transitions. The band gap energies were calculated to be 2.98 eV for FST and 1.15 eV for Ti_3AlC_2 (Fig. 8(b)),[43] suggesting that FST, with its narrow band gap, is well-suited for visible light illumination. Conversely, Ti_3AlC_2 displayed a linear trend in the UV-vis plot, indicating its dark color and its efficient absorption of visible light.[50] Fig. S4 (ESI†) presents the Tauc plot of both FST and Ti_3AlC_2 powder catalysts, respectively.

PL spectroscopy was utilized to analyze the rate of charge carrier recombination in the synthesized samples using an excitation wavelength of 325 nm. Ti_3AlC_2 exhibited strong emission intensity (Fig. 8(c)), signifying the swift recombination of photogenerated charge carriers, which aligns with its UV-vis spectrum and the linear relation for the band gap (merely 1.15 eV), suggesting the material's dark color is the primary reason for its sole absorption in the visible light region.[51] In general, typical lower peak emission in PL spectra suggests significant charge separation, leading to a decreased rate of electron–hole pair recombination. The PL intensity peak of FST was particularly low because of the minimal recombination rate of photogenerated charge carriers, finely tuned, optimized electronic properties, and narrower band gap.[52] These characteristics collectively contribute to its enhanced photocatalytic degradation activity for MB.

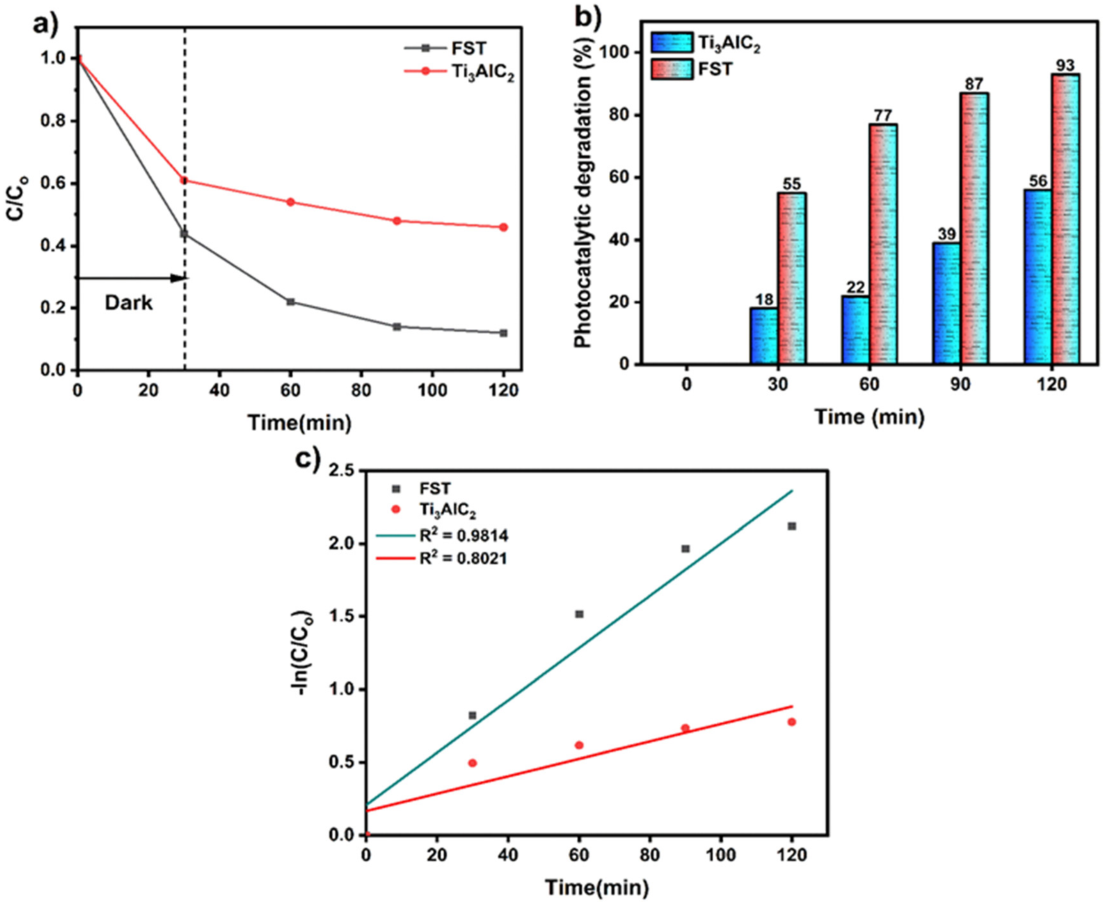

Fig. 11 (a) Photocatalytic activities, (b) degradation efficiency and (c) reaction kinetics of the as-synthesized FST and Ti_3AlC_2 powder catalysts for MB.

3.3. Photocatalytic performance

Fig. 9(a), (b) and 10(a), (b) display the UV-visible spectra illustrating the photocatalytic degradation efficiency of FST and Ti_3AlC_2. Methylene blue (MB) and rhodamine B (RB) were utilized as model pollutants, with their peak absorption intensity occurring at 664 nm and 567 nm under visible light irradiation. These peak intensities are attributed to the presence of the azo functional group (–N=N–) in the chemical structure of MB and RB. The reaction proceeded for 120 minutes, during which MB and RB degraded photocatalytically, leading to a gradual decline in absorption intensity. The degradation ratio was calculated by comparing the reduction in peak absorption intensity with the initial concentration of MB and RB. The photocatalytic degradation ratios were approximately 93% for FST and 56% for Ti_3AlC_2 powder, and in the case of RB, the degradation efficiency of FST reached a maximum value of 97% indicating that FST serves as a stable and effective photocatalyst for the degradation of MB and RB.

The results shown in Fig. 11 and 12(a) further specify the photocatalytic removal efficiencies of the FST and Ti_3AlC_2 powder samples. A graph was constructed showing the decrease in concentration (C/C_o) over time. It is evident from Fig. 11 and 12(a) that the decrease in concentration was more pronounced in the presence of light compared to darkness. This can be attributed to the adsorption-assisted photodegradation of both samples. Furthermore, during the initial 30 minutes in the absence of light, there was no discernible degradation performance. However, once reaching equilibrium and subsequently switching on the light, the performance improved significantly. 55% increase in the degradation efficiency of FST for MB and only 18% increase for the Ti_3AlC_2 powder sample were achieved. For RB, 45% improvement in degradation efficiency was achieved for FST and only 7% for the Ti_3AlC_2 powder sample. Fig. 11 and 12(b) illustrate that after 90 min of light irradiation, the maximum degradation efficiency reached 93% for FST and 56% for Ti_3AlC_2 and maximum degradation efficiencies of 96% for FST and 74% for Ti_3AlC_2 are achieved and depicted in the bar graph. These results confirm that the photocatalytic activity of FST is way better than that of Ti_3AlC_2. This superiority can be attributed to FST's lower recombination rate of photogenerated charge carriers and narrower band gap. These factors result in fewer obstacles to trapping electrons, ultimately leading to superior photocatalytic degradation performance. Furthermore, the UV-vis absorbance data were subjected to further analysis to determine the rate constant and to fit pseudo-order kinetics linearly, as illustrated in Fig. 11 and 12(c). The FST and Ti_3AlC_2 powder samples exhibited well-fitted first-order kinetics (plotting between $-\ln C_o/C$ and time), with the highest values of R^2 being 0.9814 and 0.8021 for FST and Ti_3AlC_2, respectively which further confirms the superior photocatalytic degradation efficiency of FST compared to Ti_3AlC_2.

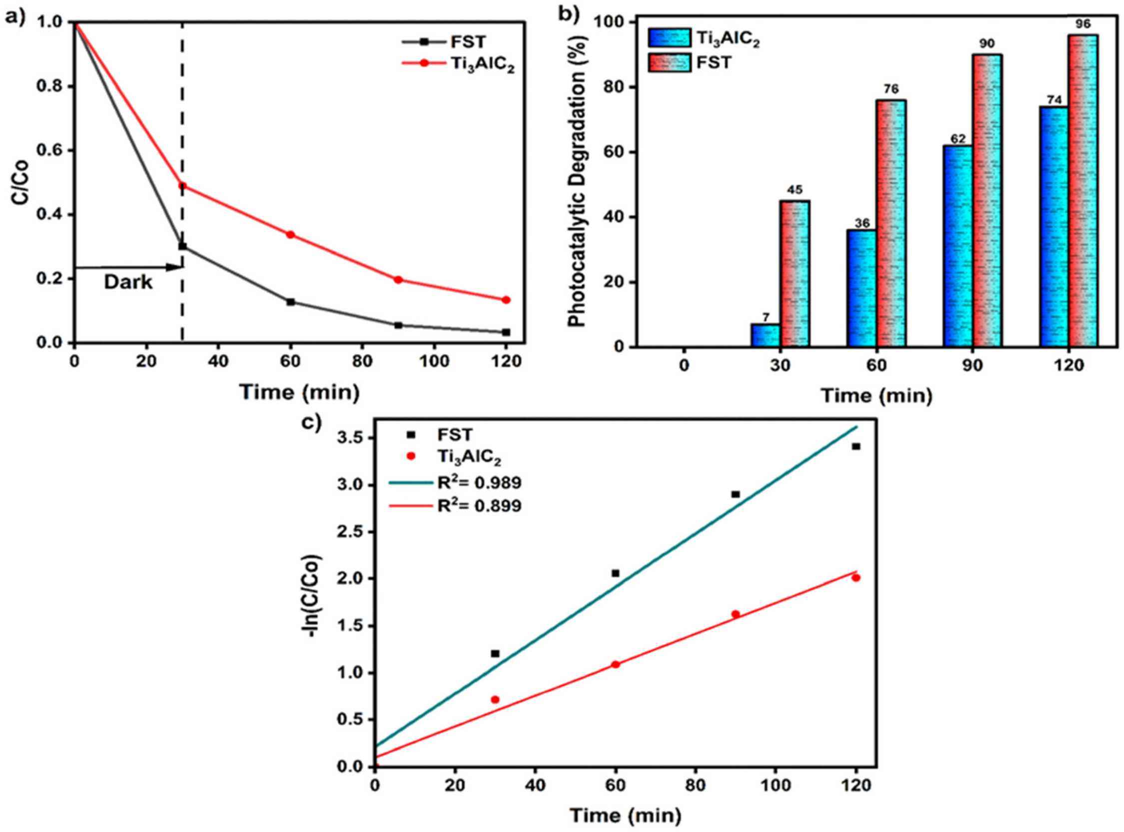

Fig. 12 (a) Photocatalytic activities, (b) degradation efficiency and (c) reaction kinetics of the as-synthesized FST and Ti_3AlC_2 powder catalysts for RB.

Furthermore, FST exhibits a band gap of approximately 2.98 eV, which aligns well with the visible light spectrum, enhancing its ability to generate electron–hole pairs upon light absorption. This narrower band gap facilitates the efficient utilization of visible light, thereby increasing the generation of reactive oxygen species crucial for the degradation of organic pollutants. The high reactivity and lower recombination rate observed in the photoluminescence spectra corroborate with the high degradation efficiencies of 93% for MB and 96% for RB under visible light conditions.

In contrast, Ti_3AlC_2, with a significantly smaller band gap of 1.15 eV, exhibits different photophysical properties. Despite its ability to absorb a broader range of visible light, the rapid recombination of photogenerated charge carriers, as indicated by its photoluminescence emission intensity, suggests less efficient photocatalytic activity. This is evidenced by its lower degradation efficiencies of 56% for MB and 74% for RB. The relationship between the band gap and the photocatalytic activity highlights the crucial role of engineered electronic properties in optimizing the photocatalytic performance. These insights are fundamental in guiding the design and synthesis of more effective photocatalysts for environmental remediation applications.

3.4. Role of scavengers and reusability studies

Considering the above results, we opted for FST as our model photocatalyst due to its superior photocatalytic performance. Tests were conducted to identify the radical species produced during photocatalyst activation (*i.e.*, $O_2^{-\bullet}$, $^{\bullet}OH$, and h^+), as these species play a crucial role in the photocatalytic process.[53] Three radical scavengers were adopted (BQ, IPA, and TEOA) with the optimized FST sample to investigate the contribution of active radicals to the photocatalytic degradation of MB into smaller products.[54] Fig. 13(a) shows the degradation percentage decreased from 93% (blank) to 42.3% upon addition of BQ as a (O_2^-) scavenger. This demonstrates the significant role of O_2^- radicals in the degradation of organic pollutants. The introduction of IPA also influenced the photocatalytic degradation of MB as an (OH^-) scavenger, resulting in a degradation rate of up to 58.5%. This notably contributed to the degradation of MB, consistent with the findings reported in the literature.[55] Furthermore, the inclusion of TEOA, acting as a (h^+) hole scavenger, led to a slight reduction in efficiency, down to 86.2%. However, it did not notably diminish the activity of the photocatalyst compared to the blank photocatalyst, indicating that holes (h^+) have the least impact on the degradation of MB.

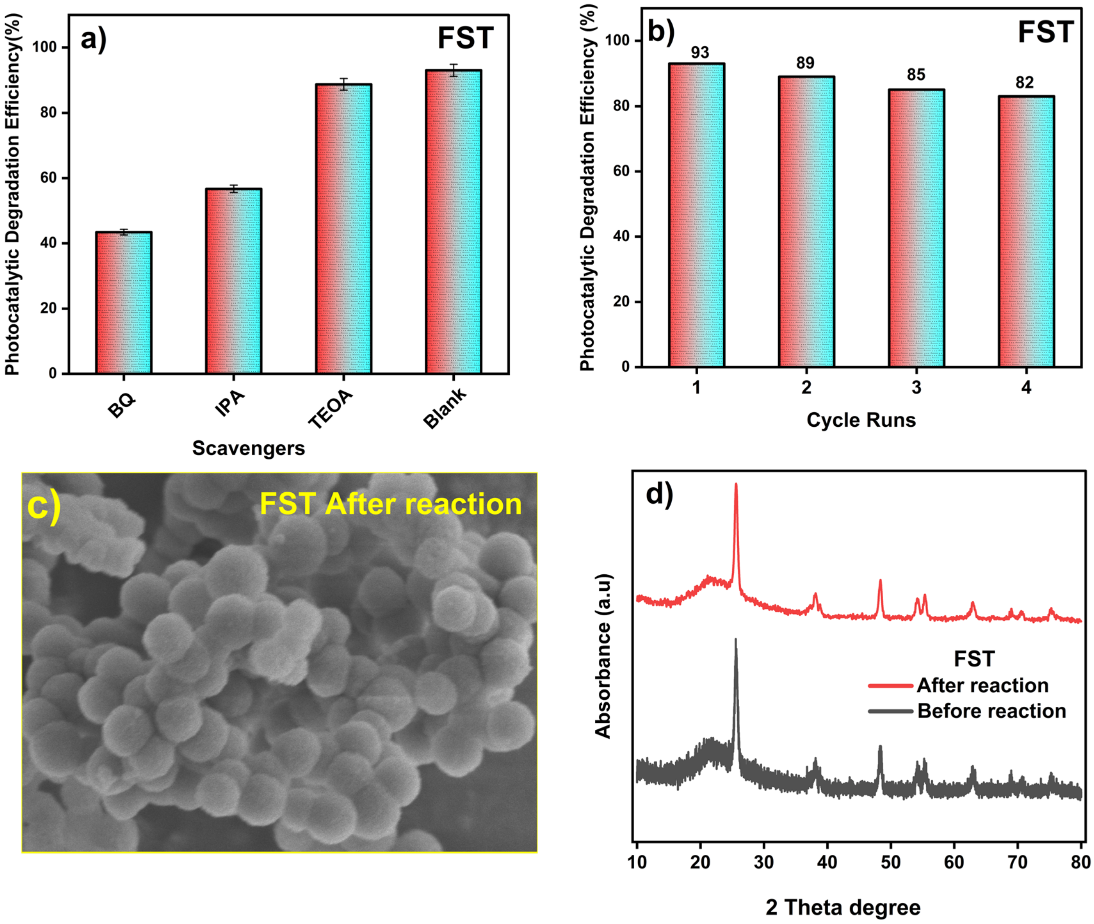

Fig. 13 (a) and (b) Scavenger studies and reusability cycle runs of the FST catalyst for MB degradation. (c) SEM image after use. (d) Before and after use XRD spectrum of FST for MB degradation.

Fig. 13(b) shows the reusability test that was conducted to assess the stability, effectiveness, and economic viability of FST as a photocatalyst. The reusability of the FST photocatalyst was tested over four cycles, and the photocatalytic activity was monitored accordingly. The photocatalytic activity of FST experienced a slight reduction, potentially due to the breakdown of MB into intermediates and the agglomeration of FST particles. This aggregation, in turn, could hinder visible light irradiation. However, even after four cycles, FST maintained over 80% of its photocatalytic activity, suggesting that it can be effectively reused multiple times for MB dye photodegradation, offering an economically feasible, stable, and efficient performance. A key benefit of the FST photocatalyst is its lightweight nature, allowing for easy recovery post-use through a simple drying process. Fig. 13(c and d) depicts the SEM image and XRD spectra of the FST photocatalyst after four regeneration cycles, which remained comparable to its initial state. This highlights the high stability and reusability of the FST photocatalyst for photocatalytic applications.

3.5. GC-MS analysis

GC-MS analysis was performed to examine the intermediate products generated during the photocatalytic degradation of MB. Fig. 14 illustrates the degradation pathway of MB under visible light irradiation. Initially, the (•OH) radicals primarily target the N–S heterocyclic group structure.[56] The degradation proceeds with the formation of 2-amino-5-dimethylamino-benzenesulfonic acid anion and dimethyl-(4-nitro-phenyl)-amine. Subsequently, the dimethyl-(4-nitro-phenyl)-amine was captured by hydroxyl radicals, resulting in the formation of *p*-dihydroxy benzene. Furthermore, the 2-amino-5-dimethylamino-benzenesulfonic acid anion continued to be broken into 4-amino-benzenesulfonic acid and 2-amino-5-dimethylamino-benzenesulfonic acid. Ultimately, the 4-nitro-benzenesulfonic acid anion undergoes direct attack and subsequent degradation, yielding CO_2 and H_2O through a sequence of reactions. This process bears a resemblance to the degradation mechanism observed in methylene blue when subjected to atmospheric pressure dielectric barrier discharge plasma.[57]

3.6. Electrochemical characteristics

To further confirm the reduction in recombination of photogenerated electron–hole pairs, electrochemical impedance spectroscopy was carried out for the FST and Ti_3AlC_2 powder samples as depicted in Fig. 15(a), and it was observed that the arc radius in the case of FST was quite smaller than that of the Ti_3AlC_2 powder sample which contributes to the more efficient way of conducting electrons. This shows that the FST catalyst has better stability for electron transfer and can transfer more rapidly. Fig. 15(b) presents the transient photocurrent responses and the relative intensities of FST and Ti_3AlC_2 powder samples. It can be seen from Fig. 15(b) that the photocurrent intensity of FST is relatively higher compared to that of the Ti_3AlC_2 powder sample. The lower emission peak, smaller arc radius and high current intensity confirm that FST can be used as an effective photocatalyst for the degradation of MB and RB. Fig. 15(c) shows the chrono-potentiometric stability curves of FST and Ti_3AlC_2 powder samples, indicating minimal voltage loss and greater stability for FST. This further reinforces the superior stability and efficiency of FST as a photocatalyst.

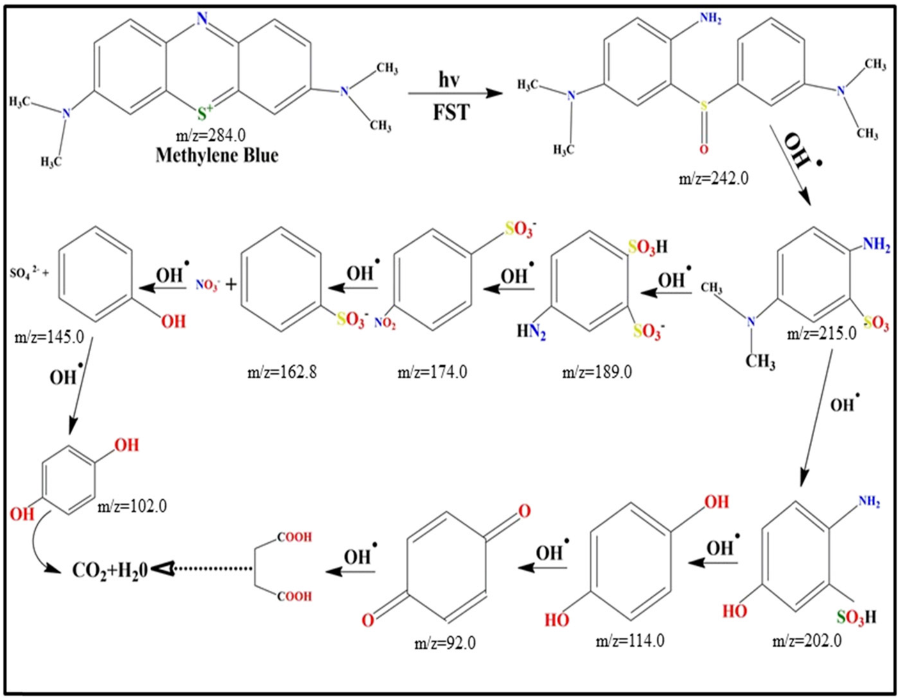

Fig. 14 Proposed degradation route of the as-synthesized FST catalyst for MB.

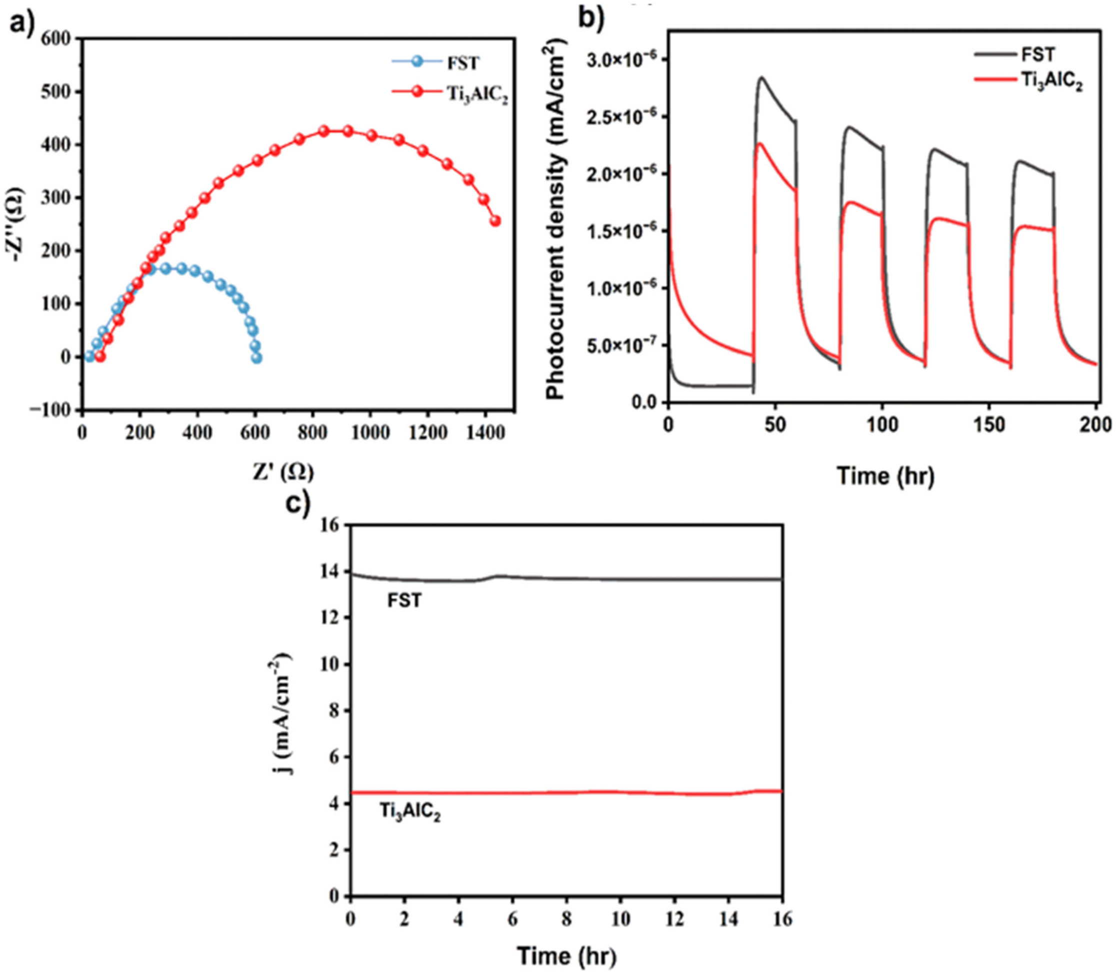

Fig. 15 (a) Electrochemical impedance spectroscopy (EIS) of FST and Ti_3AlC_2 powder samples, (b) transient photocurrent responses and (c) chronopotentiometric analysis of FST and Ti_3AlC_2 powder samples.

3.7. Proposed photocatalytic mechanism

The degradation of organic pollutants such as MB and RB through photocatalysis relies on robust redox reactions involving highly reactive species like hydroxyl radicals ($OH^\bullet$) and superoxide radicals ($O_2^{-\bullet}$). In this study, the photogenerated charge carriers from the FST photocatalyst facilitate the production of $O_2^{-\bullet}$ and $^\bullet OH$, which actively participate in the degradation of MB and RB. On exposure to the light, electron–hole pairs are generated on the surface of the FST photocatalyst, eqn (3). These photogenerated electrons, present in the conduction band of FST, interact with adsorbed O_2 molecules, resulting in the formation of $O_2^{-\bullet}$ radicals.[58] These radicals serve as a conductive pathway for electrons, effectively reducing the recombination process as outlined in eqn (4). The holes present in the valence band of FST can react with the hydroxyl ions (OH^-) present in the solution of MB and RB and form the hydroxyl radicals eqn (5).[59,60] Both $^\bullet OH$ and $O_2^{-\bullet}$ radicals exhibit high reactivity towards the MB and RB dyes, facilitating their degradation into less toxic compounds such as H_2O and CO_2 (eqn (6) and (7)). This proves that the generation of $O_2^{-\bullet}$ and $^\bullet OH$ radicals serves as the main driving force in the

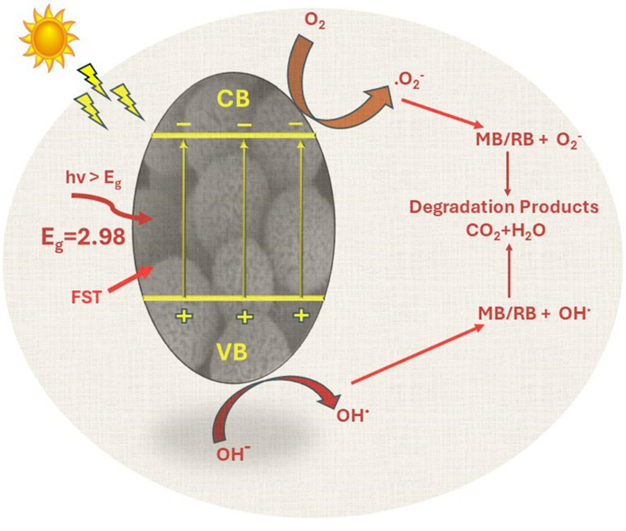

Fig. 16 Proposed photocatalytic degradation mechanism of the FST catalyst.

photocatalytic degradation of MB and RB. The proposed mechanism for MB and RB degradation is illustrated in Fig. 16.

$$\mathrm{FST} + h\nu = \mathrm{e_{CB}}^{-} + \mathrm{h_{VB}}^{+} \tag{3}$$

$$\mathrm{O_2} + \mathrm{e_{CB}} \rightarrow \mathrm{O_2}^{\bullet -} \tag{4}$$

$$\mathrm{FST(h_{VB}}^{+}) + \mathrm{OH}^{-} \rightarrow \mathrm{OH}^{\bullet} \tag{5}$$

$$\mathrm{MB/RB} + \mathrm{OH}^{\bullet} \rightarrow \mathrm{CO_2} + \mathrm{H_2O} + \text{degradation products} \tag{6}$$

$$\mathrm{MB/RB} + \mathrm{O_2}^{\bullet -} \rightarrow \mathrm{CO_2} + \mathrm{H_2O} + \text{degradation products} \tag{7}$$

4. Conclusion

In conclusion, this study provided a comprehensive comparison of synthesized fibrous silica titania and Ti_3AlC_2 through detailed characterization and photocatalytic performance evaluation. Comprehensive characterization techniques, including XRD, SEM, TEM, XPS, UV-vis, PL spectroscopy, BET, FTIR and ESR, revealed the superior properties of FST. The FST catalyst exhibited remarkable photocatalytic activity, achieving degradation efficiencies of 93% for methylene blue and 96% for rhodamine B under visible light, significantly outperforming Ti_3AlC_2, which showed lower efficiencies of 56% for MB and 74% for RB. The enhanced performance of FST is attributed to its lower recombination rate of photogenerated charge carriers and a narrower band gap of approximately 2.98 eV.

Reusability and radical scavenger tests confirmed the stability and efficiency of FST as a photocatalyst. Additionally, GC-MS analysis provided insights into the degradation intermediates, showing that they are ultimately converted into harmless products. Due to its reusability and stability, and harmlessness of its degradation intermediates, FST is considered to be able to provide a cost-effective and eco-friendly photocatalytic pathway of pollutants. These findings establish FST as a promising and efficient photocatalyst for sustainable wastewater treatment and organic pollutant degradation.

Data availability

The author confirms that the data supporting the finding of this study are available within the article and its supplementary material. Raw data that support the findings of this study are available from the corresponding author, upon reasonable request.

Conflicts of interest

The authors declare that they have no known competing financial interests or personal relationships that could have appeared to influence the work reported in this paper.

Acknowledgements

The authors gratefully acknowledge the financial support from the National Natural Science Foundation of China (grant No. 62375200, grant No. 61975148).

References

1 F. Ghanbari and M. Moradi, Application of peroxymonosulfate and its activation methods for degradation of environmental organic pollutants, *Chem. Eng. J.*, 2017, **310**, 41–62.

2 Y. Peng, H. Tang, B. Yao, X. Gao, X. Yang and Y. Zhou, Activation of peroxymonosulfate (PMS) by spinel ferrite and their composites in degradation of organic pollutants: *A Review*, *Chem. Eng. J.*, 2021, **414**, 128800.

3 S. Barışçı, F. Ulu, M. Sillanpää and A. Dimoglo, Evaluation of flurbiprofen removal from aqueous solution by electrosynthesized ferrate (VI) ion and electrocoagulation process, *Chem. Eng. J.*, 2015, **262**, 1218–1225.

4 M. Usman, K. Imran Khan, M. Adnan and A. Khan, Facile synthesis of NiAl-LDH/Ag/g-C_3N_4 ternary composite for photocatalytic degradation of methylene blue, *Fullerenes, Nanotubes Carbon Nanostruct.*, 2023, **32**, 264–273.

5 F. Saeed, M. Ahmad, A. Zada, D. Qi and Y. Wang, Phosphorus-doped $CoFe_2O_4$ nanoparticles decorated nitrogen-doped graphene for efficient and stable electrocatalytic water splitting, *Int. J. Hydrogen Energy*, 2024, **59**, 1196–1204.

6 S. R. Pouran, A. A. Aziz and W. M. A. W. Daud, Review on the main advances in photo-Fenton oxidation system for recalcitrant wastewaters, *J. Ind. Eng. Chem.*, 2015, **21**, 53–69.

7 N. C. Cinperi, E. Ozturk, N. O. Yigit and M. Kitis, Treatment of woolen textile wastewater using membrane bioreactor, nanofiltration and reverse osmosis for reuse in production processes, *J. Cleaner Prod.*, 2019, **223**, 837–848.

8 A. Lepland, T. J. Andersen, A. Lepland, H. P. H. Arp, E. Alve, G. D. Breedveld and A. Rindby, Sedimentation and chronology of heavy metal pollution in Oslo harbor, Norway, *Mar. pollute. Bull.*, 2010, **60**, 1512–1522.

9 D. Chen, Y. Cheng, N. Zhou, P. Chen, Y. Wang, K. Li, S. Huo, P. Cheng, P. Peng and R. Zhang, Photocatalytic degradation of organic pollutants using TiO_2-based photocatalysts: A review, *J. Cleaner Prod.*, 2020, **268**, 121725.

10 S. Liu, Y. Yang, W. Xiao, S. Xia, C. Jin, W. Wang, S. Li, M. Zhong, S. Wang and C. Chen, Metal-organic frameworks derived porous MoS_2/CdS heterostructure for efficient photocatalytic performance towards hydrogen evolution and organic pollutants, *Int. J. Hydrogen Energy*, 2023, **48**, 32729–32738.

11 Y.-W. Kim, J.-H. Kim, D. H. Moon and H.-J. Shin, Adsorption and precipitation of anionic dye Reactive Red 120 from aqueous solution by aminopropyl functionalized magnesium phyllosilicate, *Korean J. Chem. Eng.*, 2019, **36**, 101–108.

12 S. Giannakis, K.-Y. A. Lin and F. Ghanbari, A review of the recent advances in the treatment of industrial wastewaters

by Sulfate Radical-based Advanced Oxidation Processes (SR-AOPs), *Chem. Eng. J.*, 2021, **406**, 127083.

13 D. S. Mallya, G. Yang, W. Lei, S. Muthukumaran and K. Baskaran, Functionalized MoS2 nanosheets enabled nanofiltration membrane with enhanced permeance and fouling resistance, *Environ. Technol. Innov.*, 2022, **27**, 102719.

14 Y. Mao, B. Qiu, P. Li, X. Liu and S.-M. Chen, Ultrasonic-assisted synthesis Zn0. 78Cd0. 22S/Bi_2MoO_6 heterojunction to improve photocatalytic performance for hexavalent chromium removal and hydrogen peroxide production, *Colloids Surf., A*, 2022, **648**, 129363.

15 H. Mohan, V. Ramalingam, A. Adithan, K. Natesan, K.-K. Seralathan and T. Shin, Highly efficient visible light driven photocatalytic activity of zinc/ferrite: carbamazepine degradation, mechanism and toxicity assessment, *J. Hazard. Mater.*, 2021, **416**, 126209.

16 M. P. Yadav, N. Neghi, M. Kumar and G. K. Varghese, Photocatalytic-oxidation and photo-persulfate-oxidation of sulfadiazine in a laboratory-scale reactor: Analysis of catalyst support, oxidant dosage, removal-rate, and degradation pathway, *J. Environ. Manage.*, 2018, **222**, 164–173.

17 D. Zeng, Z. Dan, F. Qin and H. Chang, Adsorption-enhanced reductive degradation of methyl orange by $Fe_{73.3}Co_{10}$-$Si_4B_8P_4Cu_{0.7}$ amorphous alloys, *Mater. Chem. Phys.*, 2020, **242**, 122307.

18 S. M. Mirbahoush, N. Chaibakhsh and Z. Moradi-Shoeili, Highly efficient removal of surfactant from industrial effluents using flaxseed mucilage in coagulation/photo-Fenton oxidation process, *Chemosphere*, 2019, **231**, 51–59.

19 A. Kubiak, Z. Bielan, M. Kubacka, E. Gabała, A. Zgoła-Grześkowiak, M. Janczarek, M. Zalas, A. Zielińska-Jurek, K. Siwińska-Ciesielczyk and T. Jesionowski, Microwave-assisted synthesis of a TiO_2-CuO heterojunction with enhanced photocatalytic activity against tetracycline, *Appl. Surf. Sci.*, 2020, **520**, 146344.

20 Q. Wang, H. Li, X. Yu, Y. Jia, Y. Chang and S. Gao, Morphology regulated Bi_2WO_6 nanoparticles on TiO_2 nanotubes by solvothermal Sb^{3+} doping as effective photocatalysts for wastewater treatment, *Electrochim. Acta*, 2020, **330**, 135167.

21 Z. Guo, L. Wu, Y. Wang, Y. Zhu, G. Wan, R. Li, Y. Zhang, D. Qian, Y. Wang and X. Zhou, Design of dendritic large-pore mesoporous silica nanoparticles with controlled structure and formation mechanism in dual-templating strategy, *ACS Appl. Mater. Interfaces*, 2020, **12**, 18823–18832.

22 N. Bayal, R. Singh and V. Polshettiwar, Nanostructured silica–titania hybrid using dendritic fibrous nano silica as a photocatalyst, *ChemSusChem*, 2017, **10**, 2182–2191.

23 A. Fauzi, A. Jalil, N. Hassan, F. Aziz, M. Azami, T. Abdullah, M. Kamaroddin and H. Setiabudi, An intriguing Z-scheme titania loaded on fibrous silica ceria for accelerated visible-light-driven photocatalytic degradation of ciprofloxacin, *Environ. Res.*, 2022, **211**, 113069.

24 S. Tasleem, M. Tahir and Z. Y. Zakaria, Fabricating structured 2D Ti_3AlC_2 MAX dispersed TiO_2 heterostructure with Ni_2P as a co-catalyst for efficient photocatalytic H_2 production, *J. Alloys Compd.*, 2020, **842**, 155752.

25 L.-Å. Näslund, P. O. Persson and J. Rosen, X-ray Photoelectron Spectroscopy of Ti_3AlC_2, Ti_3C_2T z, and TiC Provides Evidence for the Electrostatic Interaction between Laminated Layers in MAX-Phase Materials, *J. Phys. Chem. C*, 2020, **14**, 27732–27742.

26 K. Goc, W. Prendota, L. Chlubny, T. Strączek, W. Tokarz, P. Borowiak, K. Witulska, M. Bućko, J. Przewoźnik and J. Lis, Structure, morphology and electrical transport properties of the Ti_3AlC_2 materials, *Ceram. Int.*, 2018, **44**, 18322–18328.

27 E. T. Lorenzo, Synthesis and processing of MAX phases by Powder Injection Moulding and Additive Manufacturing PhD thesis, Dialnet, 2022.

28 J. Palau, J. M. Penya-Roja, C. Gabaldon, F. Javier Álvarez-Hornos, F. Sempere and V. Martínez-Soria, UV photocatalytic oxidation of paint solvent compounds in air using an annular TiO_2-supported reactor, *J. Chem. Technol. Biotechnol.*, 2011, **86**, 273–281.

29 R. Tang, S. Xiong, D. Gong, Y. Deng, Y. Wang, L. Su, C. Ding, L. Yang and C. Liao, Ti_3C_2 2D MXene: recent progress and perspectives in photocatalysis, *ACS Appl. Mater. Interfaces*, 2020, **12**, 56663–56680.

30 M. Tahir, Enhanced photocatalytic CO_2 reduction to fuels through reforming of methane over structured 3D MAX Ti_3AlC_2/TiO2 heterojunction in a monolith photoreactor, *J. CO2 Util.*, 2020, **38**, 99–112.

31 K. Huang, C. Li and X. Meng, In-situ construction of ternary Ti_3C_2 MXene@ TiO_2/$ZnIn_2S_4$ composites for highly efficient photocatalytic hydrogen evolution, *J. Colloid Interface Sci.*, 2020, **580**, 669–680.

32 A. Fauzi, A. Jalil, M. Mohamed, S. Triwahyono, N. Jusoh, A. Rahman, F. Aziz, N. Hassan, N. Khusnun and H. Tanaka, Altering fiber density of cockscomb-like fibrous silica–titania catalysts for enhanced photodegradation of ibuprofen, *J. Environ. Manage.*, 2018, **227**, 34–43.

33 M. Azami, A. Jalil, C. Hitam, N. Hassan, C. Mamat, R. Adnan and N. Chanlek, Tuning of the electronic band structure of fibrous silica-titania with g-C_3N_4 for efficient Z-scheme photocatalytic activity, *Appl. Surf. Sci.*, 2020, **512**, 145744.

34 C. Hitam, A. Jalil, S. Triwahyono, A. Ahmad, N. Jaafar, N. Salamun, N. Fatah, L. Teh, N. Khusnun and Z. Ghazali, Synergistic interactions of Cu and N on surface altered amorphous TiO $_2$ nanoparticles for enhanced photocatalytic oxidative desulfurization of dibenzothiophene, *RSC Adv.*, 2016, **6**, 76259–76268.

35 F. Aziz, A. Jalil, N. Hassan, C. Hitam, A. Rahman and A. Fauzi, Enhanced visible-light-driven multi-photoredox Cr (VI) and p-cresol by Si and Zr interplay in fibrous silica-zirconia, *J. Hazard. Mater.*, 2021, **401**, 123277.

36 N. Khusnun, A. Jalil, T. Abdullah, S. Latip, C. Hitam, A. Fauzi, N. Hassan, M. Aziz, A. Rahman and F. Aziz, Influence of TiO_2 dispersion on silica support toward enhanced amine assisted CO_2 photoconversion to methanol, *J. CO2 Util.*, 2022, **58**, 101901.

37 F. Aziz, A. Jalil, S. Triwahyono and M. Mohamed, Controllable structure of fibrous SiO_2–ZSM-5 support decorated with TiO_2 catalysts for enhanced photodegradation of paracetamol, *Appl. Surf. Sci.*, 2018, **445**, 84–95.

38 W. K. Pang, I. M. Low, B. O'Connor, Z.-M. Sun and K. Prince, Oxidation characteristics of Ti_3AlC_2 over the temperature range 500–900 C, *Mater. Chem. Phys.*, 2009, **117**, 384–389.

39 H. Liu, Y. Wang, L. Yang, R. Liu and C. Zeng, Synthesis and characterization of nanosized Ti_3AlC_2 ceramic powder by elemental powders of Ti, Al, and C in molten salt, *J. Mater. Sci. Technol.*, 2020, **37**, 77–84.

40 N. Yaacob, A. F. Ismail, G. P. Sean and N. A. M. Nazri, Structural and photocatalytic properties of co-doped hybrid ZrO_2–TiO_2 photocatalysts, *SN Appl. Sci.*, 2019, **1**, 1–14.

41 L. Chen, X. Ye, S. Chen, L. Ma, Z. Wang, Q. Wang, N. Hua, X. Xiao, S. Cai and X. Liu, Ti_3C_2 MXene nanosheet/TiO_2 composites for efficient visible light photocatalytic activity, *Ceram. Int.*, 2020, **46**, 25895–25904.

42 Q. Xu, J. Yu, J. Zhang, J. Zhang and G. Liu, Cubic anatase TiO $_2$ nanocrystals with enhanced photocatalytic CO $_2$ reduction activity, *Chem. Commun.*, 2015, **51**, 7950–7953.

43 S. Tasleem and M. Tahir, Investigating the performance of liquid and gas phase photoreactors for dynamic H2 production over bimetallic TiO_2 and Ni2P dispersed MAX Ti_3AlC_2 monolithic nanocomposite under UV and visible light, *J. Environ. Chem. Eng.*, 2021, **9**, 105351.

44 K. Uma, S.-W. Chen, B. Krishna Kumar, C. Jeyaprabha, T. C.-K. Yang and J.-H. Lin, Enhanced photocatalytic activity of CdS nanostar decorated SiO_2/TiO_2 composite spheres and the simulation effect using FDTD model, *Ionics*, 2021, **27**, 397–406.

45 P. Zhang, Y. Li, Y. Zhang, R. Hou, X. Zhang, C. Xue, S. Wang, B. Zhu, N. Li and G. Shao, Photogenerated electron transfer process in heterojunctions: in situ irradiation XPS, *Small Methods*, 2020, **4**, 2000214.

46 L. Sun, J. Xie, L. Zhang, R. Jiang, J. Wu, L. Fan, R. Shao, Z. Chen and Z. Jin, 2D black TiO_2-x nanoplate-decorated Ti_3C_2 MXene hybrids for ultrafast and elevated stable lithium storage, *FlatChem*, 2020, **20**, 100152.

47 M. Fan, G. Fan, G. Zhang and S. Zheng, Facile synthesis and kinetic mechanism of Ag-doped TiO_2/SiO_2 nanoparticles for phenol degradation under visible light irradiation, *Res. Chem. Intermed.*, 2020, **46**, 1127–1139.

48 W. Y. Chen, X. Jiang, S.-N. Lai, D. Peroulis and L. Stanciu, Nanohybrids of an MXene and transition metal dichalcogenide for selective detection of volatile organic compounds, *Nat. Commun.*, 2020, **11**, 1302.

49 M. Tahir, Construction of a stable two-dimensional MAX supported protonated graphitic carbon nitride (pg-C_3N_4)/Ti_3AlC_2/TiO_2 Z-scheme multiheterojunction system for efficient photocatalytic CO2 reduction through dry reforming of methanol, *Energy Fuels*, 2020, **34**, 3540–3556.

50 J. Kuang, Z. Xing, J. Yin, Z. Li, Q. Zhu and W. Zhou, Surface plasma Ag-decorated single-crystalline TiO_2- x (B) nanorod/defect-rich g-C_3N_4 nanosheet ternary superstructure 3D heterojunctions as an enhanced visible-light-driven photocatalyst, *J. Colloid Interface Sci.*, 2019, **542**, 63–72.

51 Y. Li, L. Ding, Y. Guo, Z. Liang, H. Cui and J. Tian, Boosting the photocatalytic ability of g-C3N4 for hydrogen production by Ti_3C_2 MXene quantum dots, *ACS Appl. Mater. Interfaces*, 2019, **11**, 41440–41447.

52 M. Peñas-Garzón, A. Gómez-Avilés, C. Belver, J. Rodriguez and J. Bedia, Degradation pathways of emerging contaminants using TiO_2-activated carbon heterostructures in aqueous solution under simulated solar light, *Chem. Eng. J.*, 2020, **392**, 124867.

53 B. Kaur, L. Kuntus, P. Tikker, E. Kattel, M. Trapido and N. Dulova, Photo-induced oxidation of ceftriaxone by persulfate in the presence of iron oxides, *Sci. Total Environ.*, 2019, **676**, 165–175.

54 H. D. Weldekirstos, T. Mengist, N. Belachew and M. L. Mekonnen, Enhanced photocatalytic degradation of methylene blue dye using facility synthesized g-C_3N_4/$CoFe_2O_4$ composite under sunlight irradiation, *Results Chem.*, 2024, **7**, 101306.

55 M. Abdullah, J. Iqbal, M. S. U. Rehman, U. Khalid, F. Mateen, S. N. Arshad, A. G. Al-Sehemi, H. Algarni, O. A. Al-Hartomy and T. Fazal, Removal of ceftriaxone sodium antibiotic from pharmaceutical wastewater using an activated carbon-based TiO_2 composite: Adsorption and photocatalytic degradation evaluation, *Chemosphere*, 2023, **317**, 137834.

56 X.-q Wang, S.-f Han, Q.-w Zhang, N. Zhang and D.-d Zhao, Photocatalytic oxidation degradation mechanism study of methylene blue dye wastewater with GR/iTO_2, *MATEC Web Conf.*, 2018, 03006.

57 F. Huang, L. Chen, H. Wang and Z. Yan, Analysis of the degradation mechanism of methylene blue by atmospheric pressure dielectric barrier discharge plasma, *Chem. Eng. J.*, 2010, **162**, 250–256.

58 M. R. Usman, A. Prasasti, S. Islamiah, A. N. Firdaus, A. W. Marita, S. Fajriyah and E. F. Yanti, Ceftriaxone Degradation using Titanium Dioxide (TiO_2) Nanoparticles: Toxicity and Degradation Mechanism, *J. Kim. Valensi.*, 2020, **6**, 82–89.

59 N. R. Reddy, U. Bharagav, M. M. Kumari, K. Cheralathan, P. Ojha, M. Shankar and S. W. Joo, Inclusion of low cost activated carbon for improving hydrogen production performance of TiO_2 nanoparticles under natural solar light irradiation, *Ceram. Int.*, 2021, **47**, 10216–10225.

60 L. Jia, M. Arain, A. Ahmed, F. Yikai, C. Zhenda, I. Hussain, G. A. Ashraf, S. B. Ahmed and H. Dai, Emerging Trends in Metal-Organic Framework (MOFs) Photocatalysts for Hydrogen Energy Using Water Splitting: A State-of-the-Art Review, *J. Ind. Eng. Chem.*, 2024, **131**, 54–135.